# Dynamic modelling of prosthetic chorded mitral valves using the immersed boundary method

P.N. Watton[a], X.Y. Luo[b],*, X. Wang[c], G.M. Bernacca[a], P. Molloy[a], D.J. Wheatley[a]

[a]*Department of Cardiac Surgery, University of Glasgow, Glasgow, UK*
[b]*Department of Mathematics, University of Glasgow, Glasgow G12 8QW, UK*
[c]*Department of Mathematics, New Jersey Institute of Technology, NJ, USA*

## Abstract

Current artificial heart valves either have limited lifespan or require the recipient to be on permanent anticoagulation therapy. In this paper, effort is made to assess a newly developed bileaflet valve prosthesis made of synthetic flexible leaflet materials, whose geometry and material properties are based on those of the native mitral valve, with a view to providing superior options for mitral valve replacement.

Computational analysis is employed to evaluate the geometric and material design of the valve, by investigation of its mechanical behaviour and unsteady flow characteristics. The immersed boundary (IB) method is used for the dynamic modelling of the large deformation of the valve leaflets and the fluid–structure interactions. The IB simulation is first validated for the aortic prosthesis subjected to a hydrostatic loading. The predicted displacement fields by IB are compared with those obtained using ANSYS, as well as with experimental measurements. Good quantitative agreement is obtained. Moreover, known failure regions of aortic prostheses are identified. The dynamic behaviour of the valve designs is then simulated under four physiological pulsatile flows. Experimental pressure gradients for opening and closure of the valves are in good agreement with IB predictions for all flow rates for both aortic and mitral designs. Importantly, the simulations predicted improved physiological haemodynamics for the novel mitral design. Limitation of the current IB model is also discussed. We conclude that the IB model can be developed to be an extremely effective dynamic simulation tool to aid prosthesis design.
© 2006 Elsevier Ltd. All rights reserved.

*Keywords:* Immersed boundary; Chordae; Mitral valve; Aortic valve; Prosthetic heart valve; Static and dynamic simulations; Fluid–structure interactions

## 1. Introduction

Currently, biological (human cadaver, bovine pericardial or porcine tissues) or mechanical prosthetic valves are used for mitral valve replacement. Biological prostheses have excellent mechanical and haemodynamic properties, however they have a limited lifespan due to tissue failure and calcification. Mechanical prostheses are more durable, but are unable to replicate physiological flow conditions. These introduce high velocity jets into the blood flow, which results in elevated shear stresses, promoting platelet aggregation (King et al, 1996). Consequently, lifelong anticoagulation therapy is required to prevent thrombosis and thromboembolism. In addition, neither type of valve is specifically designed for the mitral position: these are designed for the aortic position and reversed for the mitral position, thus they do not function in a similar haemodynamic way to the native mitral valve. More importantly, they do not retain the function of the chordae, which play a significant role in the preservation of left ventricular function.

*Corresponding author. Tel.: +44 141 3304746; fax: +44 141 3304111.

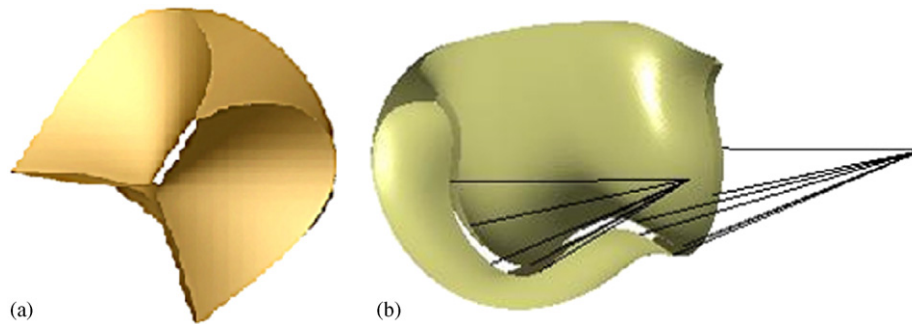*E-mail address:* x.y.Luo@maths.gla.ac.uk (X.Y. Luo).

Fig. 1. The Glasgow designed aortic (a) and chorded mitral (b) prostheses.

In this paper, a new mitral polyurethane bileaflet valve prosthesis is evaluated. It's geometry and mechanical properties are designed, to a large extent, to mimic the native mitral valve (Wheatley, 2002), see Fig. 1b. It is designed to combine the advantages of mechanical and bioprosthetic heart valves, i.e. long-term durability without the need for permanent anti-coagulation. The valve has a larger anterior leaflet and incorporates chordae, which originate from the valve annulus and traverse the leaflet, exiting at the leaflet edges to attach to the papillary muscle regions of the ventricle. The chordae act to reinforce the leaflet structure and prevent prolapse of the leaflets when the valve closes. They also help to maintain the geometry and functionality of the ventricle.

Experimental analysis, mechanical insight and experience, are integral to the development of a good valve design. Once the basic design is formulated, computational analysis can prove extremely useful: it may highlight weaknesses in the design that are not intuitive, such as locations subject to critically high stresses; material and geometric parameters may easily be varied to obtain an optimum design.

In the past, we have developed trileaflet polymer valves based on the native aortic valve design (Bernacca et al., 1995; Mackay et al., 1996a, b; Bernacca et al., 1996, 1997a, b, 1999, 2002; Wheatley et al., 2000). These designs showed potential, but some issues remained in balancing the conflicting requirements of good hydrodynamic function and excellent durability. A material that is sufficiently flexible to provide competitive hydrodynamic function (Bernacca et al., 2004) may not have the required durability due to its low modulus. A higher modulus material may be durable but may require manipulation of the design or the leaflet thickness distribution to provide competitive hydrodynamics. Optimisation of hydrodynamic function would reduce the incidence of thrombogenesis, minimising the likelihood of failure associated with leaflet stenosis due to thrombus deposition and/or calcification.

To effectively assist prosthesis design we need to consider both a static analysis, to study the mechanical behaviour of valves under peak loading conditions (systolic pressure), and a dynamic analysis with large deformation fluid–structure interactions, to study the properties of the flow though the valve, and the dynamic behaviour of the leaflets. Although there are a limited amount of static and quasi-static simulations on mitral valves (Kunzelman and Cocharan, 1993; Kunzelman et al., 1996), to the best of our knowledge, to date no work has been carried out for simulating chorded mitral valves in the fully fluid–structure interactive opening and closing phases. Many currently available commercial packages, e.g. ANSYS, CFX, Fluent, all have difficulty modelling the strongly coupled fluid–structure interaction (FSI) of heart valve prostheses due to the inherent large deformations and severe distortions to the fluid mesh.

In this paper, we use the immersed boundary (IB) method to simulate the FSI problem in which an elastic material interacts with a viscous incompressible fluid (Peskin, 2002). IB's effective dynamic capability has been used to model blood flow patterns in the heart (McQueen and Peskin, 1997; Peskin, 1972, 1977; Peskin and McQueen, 1995, 1996), platelet aggregation during blood clotting (Fogelson, 1984), flow and transport in a renal arteriole (Arthurs et al., 1998), wave propagation in the cochlea (Beyer, 1992), aquatic animal locomotion (Fauci and Peskin, 1988), wood pulp fibres dynamics (Stockie & Green, 1998), and to assist prosthetic valve design (McQueen and Peskin, 1983, 1985). However, it was not initially designed to consider hydrostatic loading and modelling of arbitrary geometries. This is because the IB models needed to be created from a network of interconnecting fibres whose geometries and stiffness are defined to mechanically represent the structure to be modelled. The geometry of the fibres was generally defined by equations, an impractical approach if arbitrary and complicated valve geometries are to be constructed.

We have extended the current IB method so that it can effectively model arbitrary geometries, as well as be subjected to static loading. The ability to model static loading is important, since comparisons and validation

of IB are only practical with alternative computational approaches in static loading. We have validated our approach by computationally subjecting the prostheses to systolic pressure loading and comparing the displacement and strain fields predicted by IB with those obtained using ANSYS (a finite element package). This is followed by the dynamic simulations of the trileaflet and bileaflet mitral prostheses. The pressure gradients are predicted, over a range of four physiological pulsatile flow rates, during the opening and closing phases for both prostheses. Excellent quantitative and qualitative agreement is obtained with experimental results.

## 2. Methodology

### 2.1. The immersed boundary method

The IB method considers the interaction of a viscous incompressible fluid with an immersed system of elastic fibres. The geometry and stiffness of the fibres are constructed to represent the elastic body to be modelled. Each fibre is comprised of a collection of *elastic nodal points* and connecting *elastic fibre segments*. The effect of the fibres is to transmit an additional stress to the fluid. A fixed Eulerian lattice, $\mathbf{x} = (x_1, x_2, x_3)$, describes the fluid, and a freely moving Lagrangian lattice, $\mathbf{r} = (r_1, r_2, r_3)$, the elastic material. The interaction between the solid and structure is achieved by distributing an inhomogeneous forcing term onto the fluid domains, and interpolating the velocity of the elastic body from neighbouring fluid nodes near the fluid–structure interface.

Let $\Omega$ be the domain of influence or support attached to every immersed elastic nodal point $\mathbf{X}(\mathbf{r}, t)$, along a single smooth submerged elastic fibre $\Gamma_s$. The elastic fibre point force density $\mathbf{F}(\mathbf{r}, t)$ (e.g. Peskin and McQueen, 1989) is

$$\mathbf{F}(\mathbf{r}, t) = \frac{\partial}{\partial s}(T\boldsymbol{\tau}), \tag{1}$$

where $T$ represents the tension within the fibre (which may be a nonlinear function of the fibre strain), $\boldsymbol{\tau}$ is the unit tangent vector to the fibres, $s$ is the arc length, and $t$ denotes time. Note, at a typical spatial location $A$ if $J$ fibres pass through the point $A$, then the nodal force density is

$$\mathbf{F}_A(\mathbf{x}, t) = \sum_{j=1}^{J} \mathbf{F}_A^j(\mathbf{r}, t) = \sum_{j=1}^{J} \partial(T_J \tau_A^j)/\partial s, \tag{2}$$

where $T_j$ is the tension and $\tau_A^j$ the unit vector of the $j$th fibre at the point $A$.

The nodal force density needs to be distributed to the fluid and expressed in terms of the Eulerian variables.

This is achieved (Peskin and McQueen, 1989) by expressing it as the convolution of the fibre force density with a delta function

$$\mathbf{f}(\mathbf{x}, t) = \int_{\Gamma_s} \mathbf{F}(\mathbf{r}, t)\delta(\mathbf{x} - \mathbf{X}(\mathbf{r}, t)) \, ds, \tag{3}$$

where $\mathbf{f}(\mathbf{x}, t)$ is the force density applied by the fibre to the fluid at time $t$ and $\delta$ is the 3-dimensional Dirac delta function $\delta(\mathbf{x}) = \delta(x_1)\delta(x_2)\delta(x_3)$. The integral is performed over the entire system of fibres.

The Navier–Stokes equations govern the motion of the fibre-reinforced viscous incompressible fluid, i.e.

$$\rho\left(\frac{\partial \mathbf{u}}{\partial t} + \mathbf{u} \cdot \nabla \mathbf{u}\right) + \nabla p = \mu \nabla^2 \mathbf{u} + \mathbf{f}, \quad \nabla \cdot \mathbf{u} = 0, \tag{4}$$

where $\mathbf{u}(\mathbf{x}, t)$ is the fluid velocity, $p(\mathbf{x}, t)$, the fluid pressure, and $\rho$ and $\mu$ represent the fluid density and viscosity, respectively. The no-slip condition of a viscous fluid implies that the fibres move at the same velocity as neighbouring fluid particles along the fluid structure interface and thus

$$\mathbf{u}(\mathbf{X}(\mathbf{r}, t)) = \frac{\partial \mathbf{X}(\mathbf{r}, t)}{\partial t} = \int \mathbf{u}(\mathbf{x}, t)\delta(\mathbf{x} - \mathbf{X}(\mathbf{r}, t)) \, d\mathbf{x}, \tag{5}$$

where $\mathbf{u}(\mathbf{X}(\mathbf{r}, t))$ is the velocity of the fibres.

Note, (5) implies that if two nodal elastic points on two different fibres have identical spatial coordinates at $t = 0$, then this will be true for all successive times. *Tethering fibres,* used to enforce boundary conditions, make use of this fact. These are very stiff, single segment fibres, one end of which (the anchor) has a fixed spatial location, the other end has identical coordinates with the fibre point to be constrained. If the tethered fibre point moves, a stress will be generated in the tethering fibre, acting to oppose the movement of the tethered point. Increasing the stiffness for the tethering fibre increases the spatial constraint of the tethered nodal point.

Eqs. (1)–(5) completely specify the system. The incompressible viscous Navier–Stokes equations are discretised on a fixed Eulerian lattice whilst the elastic fibre equations are discretised on a moving Lagrangian array of points, which do not necessarily coincide with the fixed Eulerian mesh points of the fluid computation. The interaction between the fibres and the fluid is handled by a smoothed approximation to the Dirac delta function used to interpolate the fluid velocity to the solid and to apply the solid force to the fluid. The adoption of a regular Eulerian lattice and the periodic boundary conditions enables a fast Fourier transform to be employed to solve the fluid equations.

### 2.2. Generating IB fibre geometries

The valve designs are created using SOLIDWORKS design software. The geometry is exported as an IGES
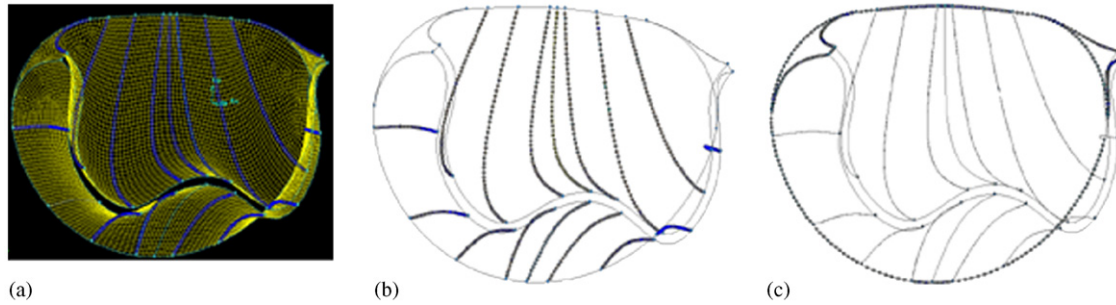
Fig. 2. Generating the fibre geometries from finite element model for (a) leaflets (b) and chordae (c) fixed boundaries of the bileaflet mitral valve.
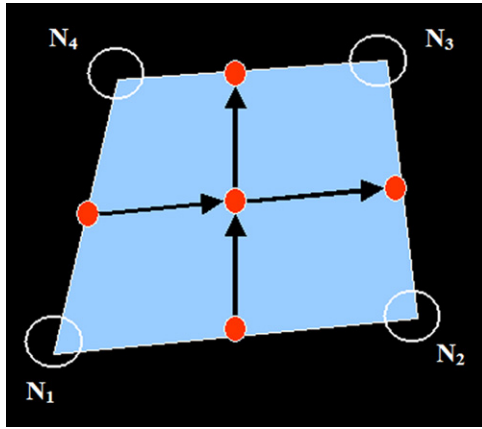


Fig. 3. Fibres are generated from the midpoints of an element and attached to one another at the centre of the element.

file and imported into GAMBIT, a mesh generating software, where the finite element discretisation is carried out. Compared with the trileaflet design, which has three similar leaflets of a homogeneous construction, the bileaflet mitral prosthesis is more complex to model. It has two leaflets of significantly different geometry and a heterogeneous structure in which the chordal components are constructed from materials of different mechanical properties to the leaflet matrix material.

The leaflets are divided into sections bordered by each chord and meshed with 4 node quadrilateral elements (Fig. 2a). This ensures that the exact geometry of the chord is modelled and that each fibre point on a chord shares identical spatial coordinates with a fibre point on the leaflet. The generated mesh files, which detail vertices, coordinates and the connectivity matrix for each leaflet are then exported from Gambit to Fortran subroutines to generate an IB fibre network consistent with the geometry and material properties of the leaflets. In each element, two fibres ($\alpha = 1, 2$) are generated from the midpoints of the sides of the element, and these fibres are attached at a fibre point in the centre of the element (see Fig. 3), i.e. each fibre consists of 3 fibre

points. If the position vectors of the element nodes are $\mathbf{N}_{(E,1)}, \mathbf{N}_{(E,2)}, \mathbf{N}_{(E,3)}, \mathbf{N}_{(E,4)}$, then the position vectors of the *elastic nodal points* are:

$$\mathbf{p}^1_{(E,1)} = (\mathbf{N}_{(E,1)} + \mathbf{N}_{(E,2)})/2,$$
$$\mathbf{p}^2_{(E,1)} = (\mathbf{N}_{(E,1)} + \mathbf{N}_{(E,2)} + \mathbf{N}_{(E,3)} + \mathbf{N}_{(E,4)})/4,$$
$$\mathbf{p}^3_{(E,1)} = (\mathbf{N}_{(E,3)} + \mathbf{N}_{(E,4)})/2,$$
$$\mathbf{p}^1_{(E,2)} = (\mathbf{N}_{(E,1)} + \mathbf{N}_{(E,4)})/2,$$
$$\mathbf{p}^2_{(E,2)} = (\mathbf{N}_{(E,1)} + \mathbf{N}_{(E,2)} + \mathbf{N}_{(E,3)} + \mathbf{N}_{(E,4)})/4,$$
$$\mathbf{p}^3_{(E,2)} = (\mathbf{N}_{(E,2)} + \mathbf{N}_{(E,3)})/2, \tag{6}$$

where $\mathbf{p}^i_{(E,\alpha)}$ is the position vector of a fibre point in an element, $\alpha = 1, 2$ denotes the fibre in the element, and $i = 1, 2, 3$ labels the *elastic nodal points*.

The stiffness of the fibres, $s$, is defined using the standard definition for a Hookean spring, i.e. $s = EA/l$, where $E$ is the Young's modulus, $A$ the cross-sectional area, and $l$ the rest length. For a general quadrilateral element, an average cross sectional area, $\tilde{A}_{(E,\alpha)}$, associated with a fibre may be defined as $\tilde{A}_{(E,\alpha)} = V_E/l_{(E,\alpha)} = h_E A_E/l_{(E,\alpha)}$, where $V_E$ is the volume, $A_E$ is the planar cross sectional area, $h_E$ the thickness of the element, and $l_{(E,\alpha)}$ the length of the fibre. Since a fibre segment is half the length of a fibre, the stiffness of each fibre segment is $s_{(E,\alpha)} = 2EhA_E/l^2_{(E,\alpha)}$.

The chordae emanate from the papillary point, attach to the leaflet edge and continue through the leaflets to the valve annulus. Fixed boundary conditions are easily implemented by attaching the *tethering fibres* to the *elastic fibre points*, which are required to be spatially constrained.

### 2.3. Element reconstruction and pressure application

The valve surface is reconstructed from the fibre representation, for post-processing. Given the position vectors of the fibre points, the associated elements can be reconstructed. The initial shape of the element is encoded, as there is insufficient information to reconstruct a general quadrilateral solely from its midpoints.

To this purpose, one of the nodal points may be expressed in terms of base vectors that describe the element.

$$\mathbf{N}_{(E,1)} = \mathbf{p}_{(E,1)}^2 + \alpha_E(\mathbf{p}_{(E,1)}^1 - \mathbf{p}_{(E,1)}^2) + \beta_E(\mathbf{p}_{(E,2)}^1 - \mathbf{p}_{(E,2)}^2)$$
$$+ \gamma_E((\mathbf{p}_{(E,1)}^1 - \mathbf{p}_{(E,1)}^2) \wedge (\mathbf{p}_{(E,2)}^1 - \mathbf{p}_{(E,2)}^2)). \quad (7)$$

The initial nodal position vectors $\mathbf{p}_{(E,\alpha)}^i(t=0)$ are known, thus the parameters $(\alpha_E, \beta_E, \gamma_E)$, can be determined for each element, by solution of (7). Given $\mathbf{p}_{(E,\alpha)}^i(t)$, the reconstruction can then be applied as the structure deforms, i.e. $\mathbf{N}_{(E,1)}$ can be calculated using (7), and the remaining nodes can be determined from (6), i.e.

$$\mathbf{N}_{(E,2)} = 2\mathbf{p}_{(E,1)}^1 - \mathbf{N}_{(E,1)}, \quad \mathbf{N}_{(E,4)} = 2\mathbf{p}_{(E,2)}^1 - \mathbf{N}_{(E,1)},$$
$$\mathbf{N}_{(E,3)} = 2\mathbf{p}_{(E,1)}^3 - \mathbf{N}_{(E,4)}. \quad (8)$$

This reconstruction enables an external pressure, $p$ to be applied to a fibre structure. An element area, $A_E$, and normal vector, $\hat{n}_E$, is associated with the fibres and thus a normal pressure force, $f_E^p = pA_E\hat{n}_E$, can be applied evenly to the fibre points in the element. If the pressure is applied slowly, then the inertial forces the fluid exerts on the fibres are negligible and a quasi-static solution for the application of an external surface pressure can be obtained.

### 2.3.1. Strain and stress

If a regular mesh is used, the easiest method is to simply consider the strains in the fibre segments. However, if the orientation of the elements in the mesh from which the fibre points were constructed is very irregular, then it may be necessary to consider geometric surface strains. This also enables an easy comparison of results with ANSYS. For this purpose, we consider the first principal strain, $\lambda_E^E$, i.e. the maximum root of the cubic, det $|(2\varepsilon_{ij}^E + 1) - \lambda_p^E \delta_{ij}| = 0$, where $\varepsilon_{ij}^E$ is the strain tensor defined in the Cartesian basis (see Appendix A for details).

Each fibre has an associated area with which it was defined, thus an approximate Piola stress can be defined with respect to the original area as $P_{(E,\alpha)} = |\mathbf{F}_{(E,\alpha)}|/\tilde{A}_{(E,\alpha)}$ where $\mathbf{F}_{(E,\alpha)}$ is the force in a fibre, i.e. the product of the stiffness and the extension of the fibre, $\mathbf{F}_{(E,\alpha)} = s_{(E,\alpha)}(\lambda_{(E,\alpha)} - 1)l_{(E,\alpha)}$.

### 2.4. The manufactured valves and the test rigs

We use a test rig that simulates the function of the left ventricle to apply physiological pressure and pulsatile flow conditions to the valves (Fisher et al., 1986). This comprises an atrial reservoir, ventricular test chamber, aortic compliance and peripheral resistance. A servo-controlled pump generates near-physiological volumetric flows (of water) through the ventricular test chamber. Four flow settings are used, ranging from $3.6 \, \mathrm{l\,min^{-1}}$ (60 bpm and 60 ml volumetric flow) to $8.0 \, \mathrm{l\,min^{-1}}$ (80 bpm and 100 ml volumetric flow), at a mean aortic pressure of 95 mmHg. Transducers sampled the flow and the atrial, ventricular, aortic and differential pressures across the valve, every 0.005 s. Hydrostatic pressures up to 240 mmHg were also applied to the aortic prosthesis (Watton et al., 2004a,b) to examine static loading behaviour experimentally. Both prosthetic valves are manufactured using polyurethane material. The trileaflet prosthetic valve leaflet (Fig. 1a) material has a Young's modulus of 15 MPa, with an average leaflet thickness of 0.125 mm. The valve frame was manufactured from PEEK polymer with an inner radius of 11.2 mm. The mitral prosthetic valve leaflet matrix material has a Young's modulus of 5.4 MPa, and an average leaflet thickness of 0.1 mm. The valve is D-shaped with a stiff frame incorporating two 7 mm support posts (Fig. 1b). As for the chordal fibres, the Young's modulus is 300 MPa, and the cross-sectional area is 0.4 mm$^2$.

### 2.5. Numerical simulations

#### 2.5.1. Static analysis

The static analysis of the valves is performed with ANSYS and IB. The valves are modelled with realistic material parameters (as specified in Section 2.4) and are subject to a systolic pressure of 16 Kpa. For IB, the whole valve model is solved within a cubic fluid domain with $64 \times 64 \times 64$ nodes, and the hydrostatic pressure is applied directly onto the valve whilst the flow boundary conditions at all sides are set to be (periodically) zero. As the nature of the IB method is to assume the valve totally embedded in the fluid, it is not possible to switch off the fluid flow, instead, incremental pressure is applied extremely slowly up to the final pressure to avoid any extra inertia effects from the fluid. In the ANSYS simulations, an IGES file of the same geometry used by the IB model is imported to generate the valve model. However, due to symmetry only a third (aortic valve) or half (mitral valve) of the geometry is solved with 4-node shell elements. 2964 elements are used for aortic valve, and 12,429 elements are used for mitral valve, and the results are mirrored to recover the whole valve geometry. The contact condition is set such that no penetration is allowed.

It is noted that it is extremely difficulty to achieve converged solutions, with ANSYS, for the original valve thickness for both valves. This is due to the shell's notorious "locking" feature when the thickness is so low and the shell changes from a bending dominated state to a membrane dominated one in the finite element simulation (Chapelle and Bathe, 2003; Bathe, 1996; Chapelle, 2005). To overcome this problem, we increased the thickness of the shell by a factor $\lambda$ whilst simultaneously decreasing the Young's modulus by the same factor $\lambda$. This ensures the stretching stiffness of the

shell remains unchanged. Here, we used $\lambda = 3.5$ ($\lambda = 4$) for the aortic (mitral) valve. This is the thinnest shell we can computer within a reasonable time; the computational time is approximately 18 CPU hours on the White Rose supergrid Titania.

Note, since only stretching stiffnesses are present in IB, the mechanical properties of the IB models do not change when modifying the Young's modulus and thickness of the valve in this manner. However, for the ANSYS model, the increase in the thickness results in a slightly greater bending stiffness, which will have the consequence of smaller deformation and strains for a given loading. However, the ANSYS model should still be able to provide a reasonable approximation to the IB model, since for the thicknesses modelled, the shell is mostly in the membrane-dominated state.

### 2.5.2. Dynamic analysis

Only the IB model is employed for dynamic simulations. The valve is modelled in a cylindrical tube of length 16 cm and radius 5.6 cm (Fig. 4), constructed from a mesh of azimuthal and axial fibres. The fluid domain is chosen to have $64 \times 32 \times 32$ nodes. It is immersed within a fluid domain, using physical parameters of water, i.e. the density is $1000 \, \text{kg/m}^3$ and the viscosity is $10^{-3} \, \text{Pas}$. The valve is positioned 1/4 of the way down the tube. The aortic housing is constructed from an interwoven mesh of radial and concentric circles of fibres, whilst the more complex D-shaped geometry of the mitral housing is generated from an FEM mesh. Stiff tethering fibres are attached to all nodal fibre points of the tube and housing to enforce boundary conditions. A periodic Poiseuille flow is prescribed, $u_{\max}(t) = 2F(t)/\pi r^2$, where $u(t)$ is the peak velocity of the parabolic flow profile, $r(t)$ is the radius of the tube and $F(t)$ is a linear interpolation of the experimental flow rates.

On average, static analysis using ANSYS and IB takes about 18 CPU hours, and dynamic simulations take 9 CPU days. All computations were executed on *Titania*, the White Rose Grid Computing node housed at Sheffield University; a cluster of 10 identical (Model V880) machines, each of which comprises eight 900 MHz UltraSparc processors configured in a shared
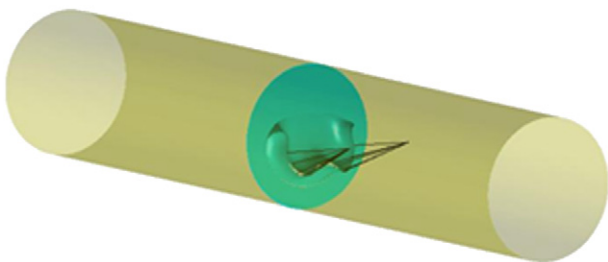


Fig. 4. The valve is housed in a cylindrical tube and subject to period velocity boundary conditions.

memory architecture. MATLAB is employed for graphical post-processing.

## 3. Results

### 3.1. Static results

Fig. 5a illustrates the deformation of the valve at a systolic pressure of 120 mmHg. Fig. 5b and c, the prediction displacements obtained using IB and ANSYS, respectively. Experimentally it is observed that the leaflet edges flatten in the central region where the 3 leaflets contact, and that there is a flattening of the belly of the leaflets. This finding is also observed with IB (Fig. 5b), although the angle the leaflets make with the commissures looks greater in IB, suggesting an over stretching of the IB model due to the lack of the bending stiffness. The flattening is less obvious in ANSYS, possibly due to a slightly increased thickness.

In the IB model there is a small break in symmetry, see Fig. 5(b). This is due to two reasons. One is that the manufactured valve itself is very slightly asymmetric, which would be reflected by the IB model. The other reason is that one of the three leaflets in IB does not share the same spatial relationship with the underlying regular cubic fluid mesh, whilst the other two do. Rotating the valve in the fluid mesh demonstrated it is always the position, rather than a particular leaflet, that undergoes the greatest deformation. This effect can be minimised by increasing the resolution of the fluid mesh, which, however, will increase the computational time significantly. Note the ANSYS model is perfectly symmetric because only a third of the valve is simulated.

The deformation distribution and magnitude is largely similar between the ANSYS and IB model, however, in ANSYS, the larger deformation area moves more towards the contact area, whilst in IB it is more towards the belly. Again, this is because the current IB model offers no bending stiffness, and it does not allow overlapping points in the solid domain, thus it can only solve the contact problem approximately.

The locations of the maximum $x$- and $y$-displacements predicted by IB and ANSYS for mitral valves are also in agreement, i.e. commissural regions of anterior leaflet (IB 0.5 mm, ANSYS 0.5 mm), and regions close to the 2nd chordae from the commisures on the porterior leaflet (IB 1.1 mm, ANSYS 1.2 mm). Both ANSYS and IB predict that the centre point of the posterior leaflet has a $y$-displacement of 1.6 mm.

The first principle strain distributions in the valve leaflets are shown for the aortic and mitral valves in Figs. 6 and 7, respectively. For aortic valve, both ANSYS (a) and IB (b) models predict the maximum principal strain near the commissure of the leaflet. The maximum values are approximately 0.28 for ANSYS,
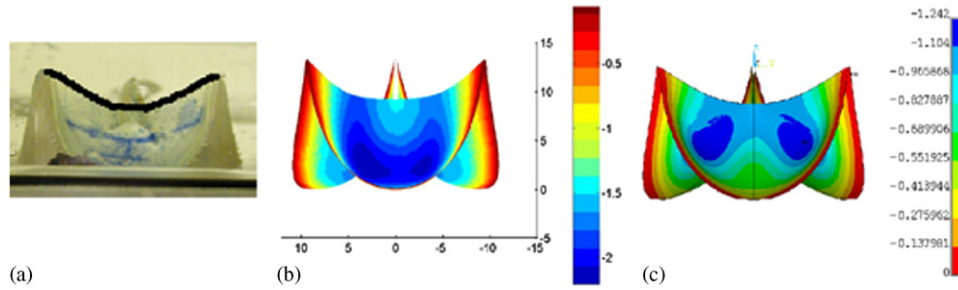
Fig. 5. (a) Deformed experimental aortic prosthesis at systolic pressure. Note, the figure has been edited to highlight the profile of the leaflet edges. Predicted vertical displacements of the aortic valve leaflets, using IB (b) and ANSYS (c). The colour bar indicates the axial displacement of valve leaflets (mm).
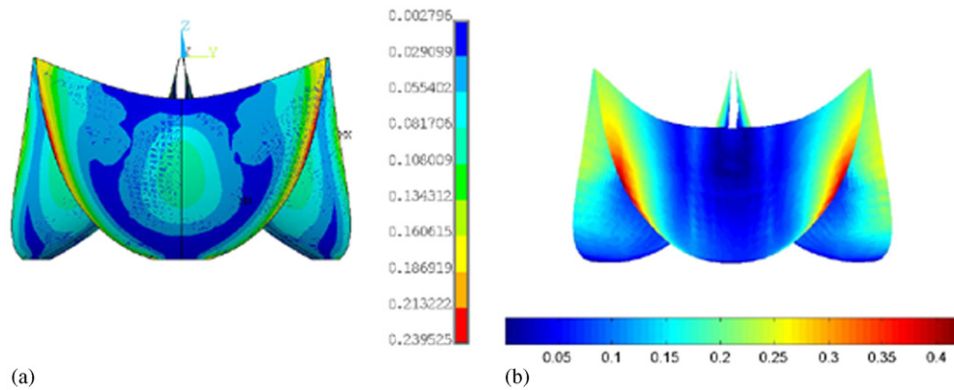


Fig. 6. Both ANSYS (a) and IB (b) models predict the maximum first principal strains to be near the commissure of the trileaflet valve.
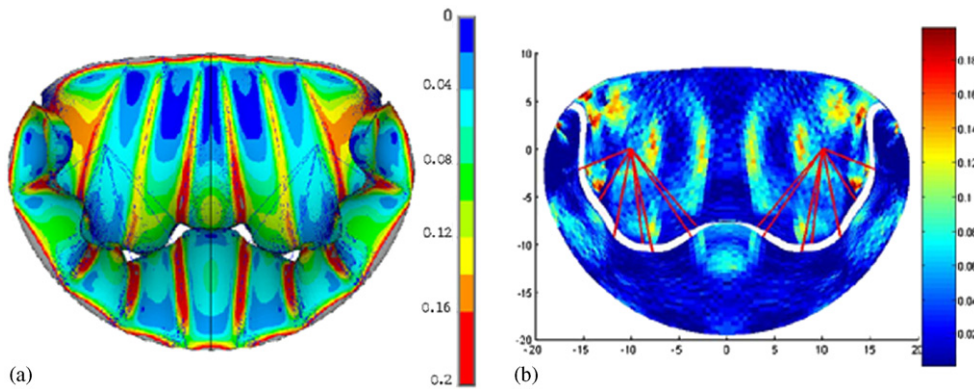


Fig. 7. The first principal strain distribution for the bileaflet valve predicted by ANSYS (a), and IB (b). Note in addition to the increased strains caused by the presence of chordae, ANSYS also predicts higher strain around the edge of the valve annlus due to bending effects.

and 0.40 for IB. Again, IB gives a slightly larger strain area than ANSYS towards the leaflet edges since the IB model cannot resist shearing. Consequently, the principal strains near the higher shear commissure region is higher than the strains experienced by the fibres: the maximum fibre strain in this location is only 0.21. For mitral valve, both IB and ANSYS predict higher strains around the chordae, the values are in the region of 10–12% around the 1st and 2nd chordae (counting from the centre) of the anterior leaflet. Higher values of the principal strain are also seen around the mitral annulus

of the ANSYS model, however, in the IB model there is no bending resistance and the leaflets are free to rotate, so these are not present.

Finally, we considered the displacement of the centre point of the three leaflets of the aortic valve as the pressure is increased to 200 mmHg (see Fig. 8). It can be seen that the predicted displacements using IB are generally in reasonable agreement with both the ANSYS and experimental measurements. ANSYS predicts a smaller deformation both compared with IB or experiments, especially at the higher pressure. IB gives much better agreement

with the experiments especially up to the systolic pressure of 120 mmHg. The lack of bending stiffness in IB becomes more noticeable at higher loading.

In general, consistent results are obtained using the three different approaches, and the IB model, being the most efficient dynamic simulation tool, is considered capable of capturing the main mechanical features of the valve.

## 3.2. Dynamic results

A physiological pulsatile flow is applied to the trileaflet and bileaflet prostheses. The pressure gradients across the valves predicted by the computational models are compared with experiment.
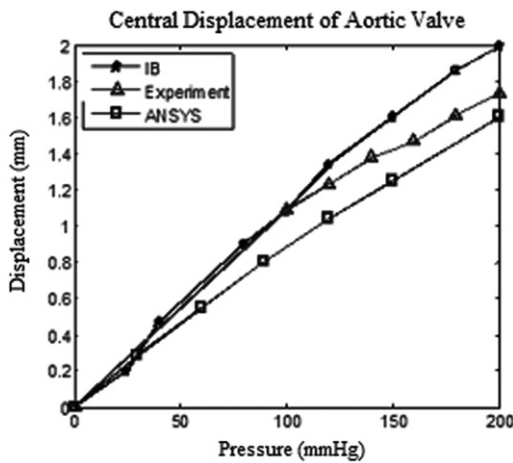
Fig. 8. The vertical displacement at the centre of the free edge of the aortic valve plotted with the static pressure.

### 3.2.1. Aortic prosthesis

The valve is tested at four physiological flow rates as before (Fig. 9a). At all flows, there is an initial and rapid increase; the flow rate then levels off briefly before a further increase up to the maximum flow rate. These flow rates approach zero with fluctuation over time, showing at least one local minimum and maximum on the way (note Flow 4 decreases to zero much more rapidly).

The experimental and computed pressure gradients across the valve are illustrated in Figs. 9b and c, respectively. It is seen that in general the pressure gradients at all flow rates agree well between the IB predictions and the experimental measurements. In experiment, the pressure gradients rise steeply to a maximum value after 0.015–0.03 s and then fall quickly to a localised minimum as the valve opens (after 0.03–0.045 s). At this point, the flow rate is still increasing, thus the pressure gradients rise again to the second maximum when the flow rate reaches its maximum. The pressure gradient then decreases with the flow rate until the secondary peak occurs (except for Flow rate 4). Finally, the pressure gradients approach zero at the onset of flow reversal.

IB model slightly over-predicts the peak opening pressure gradients for the four flow rates, i.e. 10.5, 13, 14.5, 19 mmHg compared with experimental measurements of 6.5, 8, 11, 14 mmHg. At the peak flow rate, experimental and IB pressure gradients are in good agreement, i.e. 12, 7, 5, 3 mmHg compared with experimental findings of 15, 7.5, 5, 3 mmHg.

In all simulations it is observed that the computational valves take slightly longer to open than the
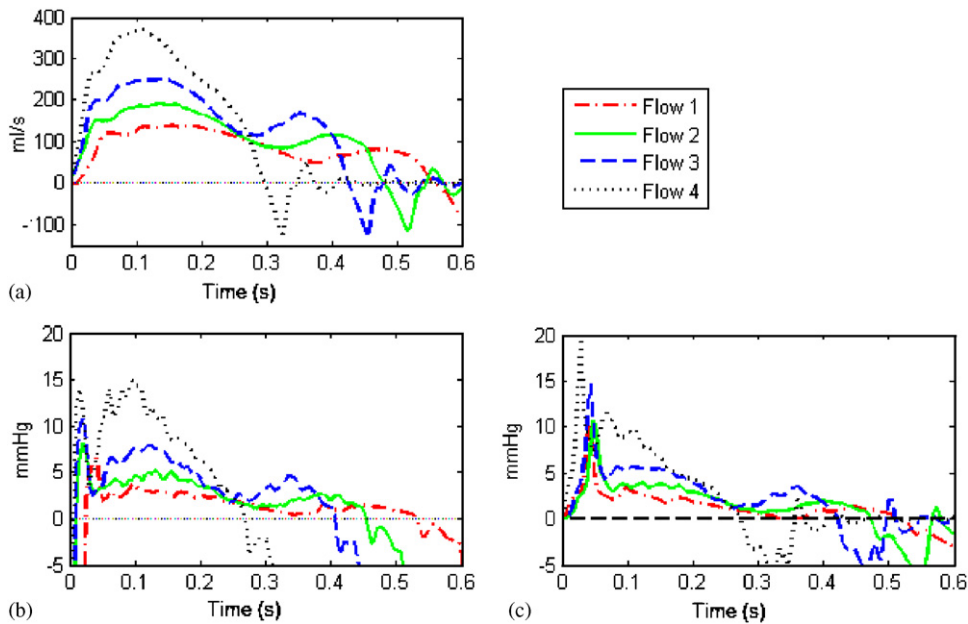
Fig. 9. (a) The experimental flow profiles for the aortic valve are prescribed as the periodic boundary conditions in IB, (b) experimental pressure gradient, and (c) IB pressure gradients (mmHg) for the aortic prosthesis.
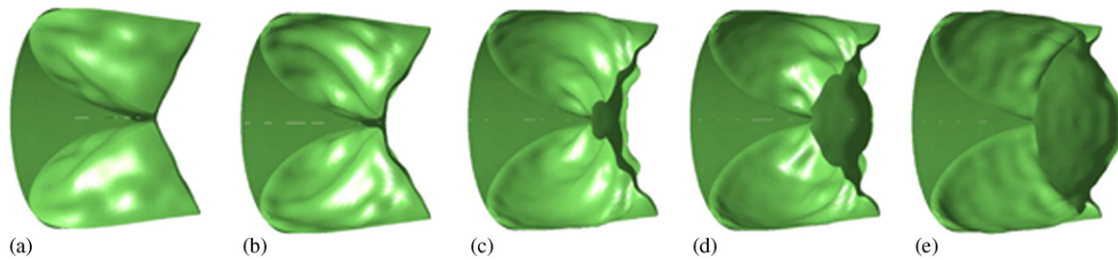
Fig. 10. Dynamic opening of the computational aortic prosthesis at time (a) $t = 0.012$ s, (b) $t = 0.024$ s, (c) $t = 0.028$ s, (d) $t = 0.032$ s, (e) $t = 0.040$ s. It is observed that the onset of opening of the leaflets begins at 0.024 s and the valve is in a fully open configuration at 0.04 s. Prior to leaflet separation, the leaflets fully inflate (b) and (c). Compare this with what is observed in experiment (Fig. 11b). For the real valve, during the onset of leaflet separation, the leaflets inflate towards the corners whilst the belly of the leaflets remains relatively sunken.
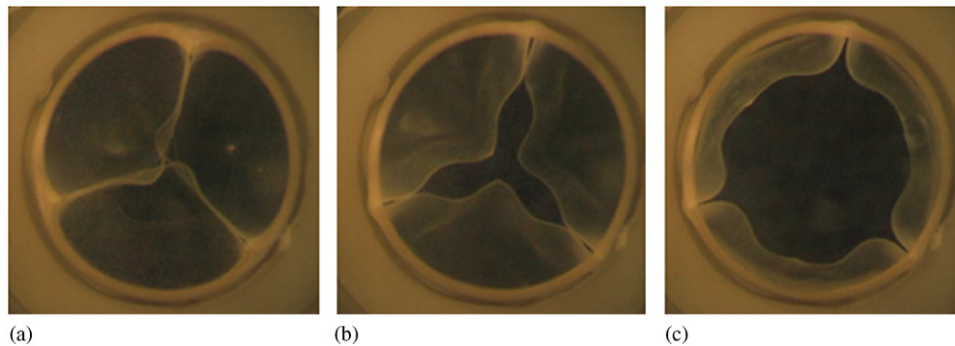


Fig. 11. Dynamic opening of the experimental aortic prosthesis: (a) closed valve (b) onset of opening (c) opened valve. Photographs were taken every 0.02 s. It was observed that the valve opened within the time of two consecutive frames, i.e. less than 0.02 s.

experimental valves. During dynamic opening using flow rate 4 (Fig. 10), the valve begins to open at $t = 0.24$ s, when the pressure gradient is at its maximum, and is fully open at 0.4 s when the pressure gradient falls to the subsequent minimum. The experimental valve opens more quickly, in approximately 0.02 s (Fig. 11). The delayed opening of the leaflets of the computational valves may be attributed to their more compliant response. In Fig. 11b, it is seen that immediately prior to opening, the experimental valve leaflets inflate in the corners and the belly of the leaflets remains sunken. Compare this with the computational model (Fig. 10c), in which the whole of the leaflets have inflated prior to leaflet separation. The obvious consequence of this is that a greater volume can be contained within the leaflets and the valve orifice prior to leaflet separation. Given that the onset of leaflet separation occurs at a later time for the computational valve, the flow rate immediately following the leaflet separation is greater. Thus the local minimum in the pressure gradient (following valve opening) is higher than that observed experimentally and consequently the second maximum in the pressure gradient is not such a noticeable feature for the computational model.

The secondary peak of the flow rate is accompanied by an increase in the pressure gradient. Quantitative consistency is found between IB and experiment here: IB

predicts the final local maxima of 5, 2.5, 1.5 mmHg for the lower three flow rates with comparable experimental values of 4, 2.5, 1.5 mmHg, respectively. The zero pressure gradients occur at similar times for IB and experiment and the slope of the pressure gradients during closure is in quantitative agreement. Note, once the flow reduces to zero the pressure gradients in IB also reduces to zero, whilst in the experimental test, systolic pressures are maintained across the prosthesis.

### 3.2.2. Mitral prosthesis

Flow profiles for the mitral prosthesis (Fig. 12a) are similar to those for the trileaflet prosthesis. The experimental pressure gradients (Fig. 12b) rise and fall less steeply than those for the trileaflet valve, i.e. the mitral leaflet separation begins later and the full opening takes longer to occur. This is associated with the more compliant response of this prosthesis, with fewer constraints on the leaflet motion. For flow rate 4, the pressure gradients then reduce to a localised minimum, increasing again as the flow rate increases. For the lower 3 flow rates, the pressure gradients fall quickly and then level off, before decreasing with the flow rate; the pressure gradients then increase again in line with the secondary peak in the flow rate before tending to zero. A local maximum is observed prior to closure of the valve for all flow rates, possibly due to leaflet compliance
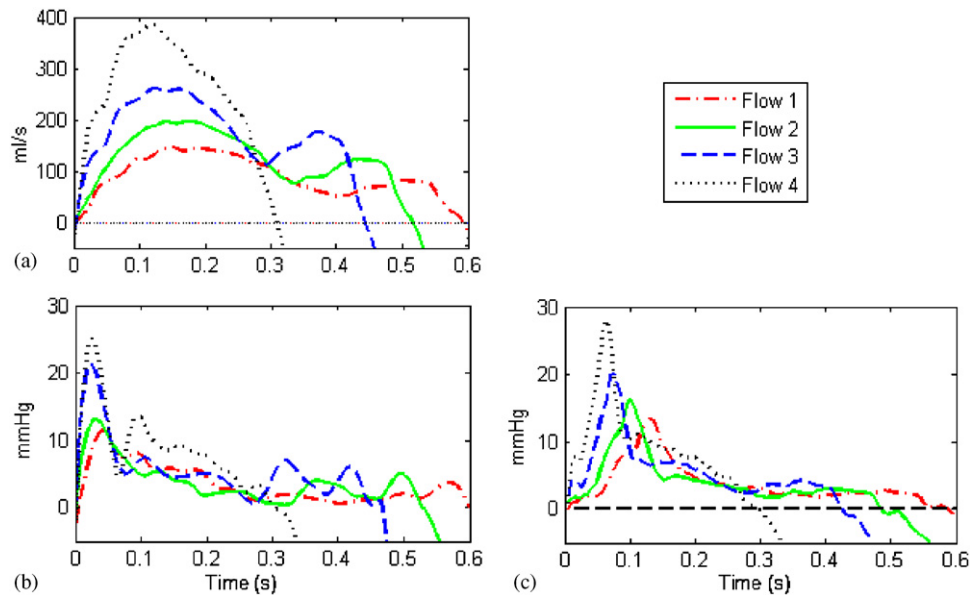
Fig. 12. (a) Experimental flow profiles for the mitral prosthesis are used as the prescribed flow rate in IB, (b) Experimental pressure gradients, and (c) IB pressure gradients (mmHg) for mitral prosthesis.

resulting in an oscillation in flow immediately prior to full closure.

Predicted peak opening pressure gradients (Fig. 12c) for the four flow rates are in quantitative agreement; 27.5, 20, 16 and 13 mmHg compared with 25, 21, 13 and 11.5 mmHg observed experimentally. Pressure gradients following opening of the mitral valve also agree with the experiments, i.e. around 10 mmHg for flow 4 and between 5 and 7.5 mmHg for the flows 1–3. Pressure gradients reduce to approximately 2–3 mmHg as the flow rate reached its minimum between 0.3 and 0.4 s. Computationally a small increase in the pressure gradients is observed when the flow reached a second local maximum, then falls as flow reverses. Experimentally, a more complex waveform is seen, with slightly higher values of pressure gradient at the secondary peak in the flow rate.

The dynamic behaviour of the valve leaflets (using flow rate 4) during the opening phase, i.e. for the first 0.1 s, is illustrated in Fig. 13. It is observed that during the first 0.06 s, the initial deformation is an inflation of the leaflets, whilst the leaflet edges remain in contact. At $t = 0.06$ s the maximum pressure gradient of 27.5 mmHg is reached, and opening of the leaflets begins. Full opening then occurs over the subsequent 0.04 s, during which time the pressure gradient across the valve falls to 11 mmHg. For this flow rate, the valve does not fully open until $t = 0.1$ s. At this time, the flow rate is almost at its maximum, and thus a subsequent constancy of the pressure gradient is observed rather than a local minimum followed by a local maximum as observed in the experiment where opening occurs earlier. It is also noted that the opening anterior leaflet deforms excessively (Figs. 13(d)–(f), 14(a)) and on closure a crimping

of the leaflet is observed (Fig. 14(b)), this shows that bending stiffness is important, especially in the these phases.

Slower opening times are observed for the IB models, i.e. 0.07–0.13 s compared with experimental findings of 0.025–0.04 s for highest to the lowest flow rates, respectively. Thus there is an appreciable delay in opening, particularly for the lower flow rates. This can be attributed to the larger inflation of the leaflets that occurs in IB prior to opening. Moreover, leaflet inflation will take longer for lower flow rates. This explains the increased delay in valve opening at lower flow rates; e.g. opening occurred 0.045 s later than the experiment for the highest flow rate, and 0.09 s later for the lowest flow rate. Note the slight delay at the slower flow rates also happens in the real valve leaflets; a small inflation occurs prior to its opening, and thus the onset of opening is marginally delayed, i.e. the location of the peak pressure gradient shifts to the right (Fig. 12b). Once the onset of leaflet separation begins, the time taken for full opening to develop is consistent with experiment: for flow 4, it is approximately 0.04 s.

Finally, we compare the velocity vector plots of the flow through the two prostheses. The trileaflet valve generates a central jet, with peak velocity in the region of 150 cm/s, and vortices are shed from the leaflet and swept downstream (Fig. 15a). The asymmetry of the mitral design resulted in an asymmetry being generated in the flow and the central jet is deflected upwards (Fig. 15b). These mitral flow dynamics are similar to those present physiologically (Daebritz et al., 2003), where a large vortex develops that completely fills the ventricle, saving the energy of the flow for the ejection. This suggests that the new mitral design will perform
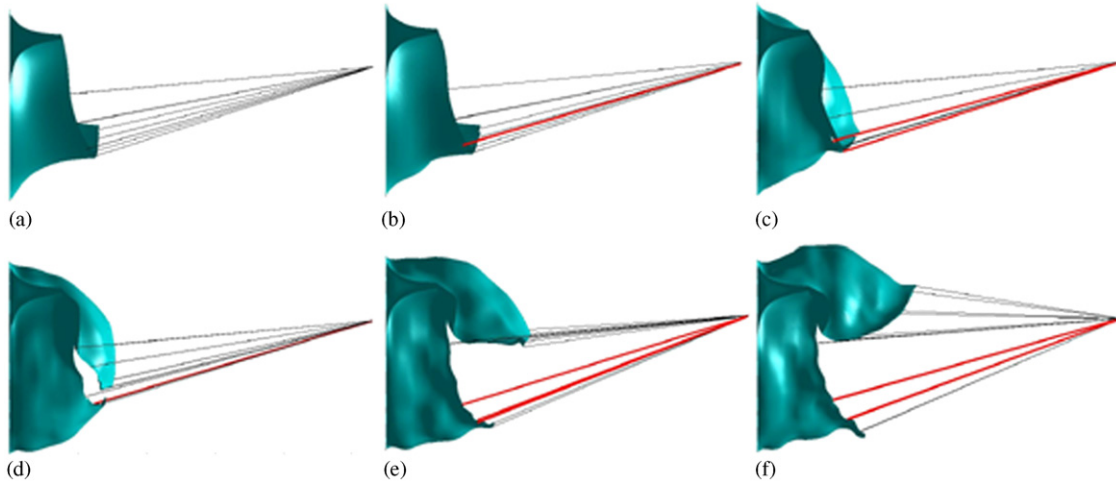
Fig. 13. Dynamic opening of mitral valve: (a) $t = 0$ s, (b) $t = 0.02$ s, (c) $t = 0.04$ s, (d) $t = 0.06$ s, (e) $t = 0.08$ s, (f) $t = 0.1$ s.
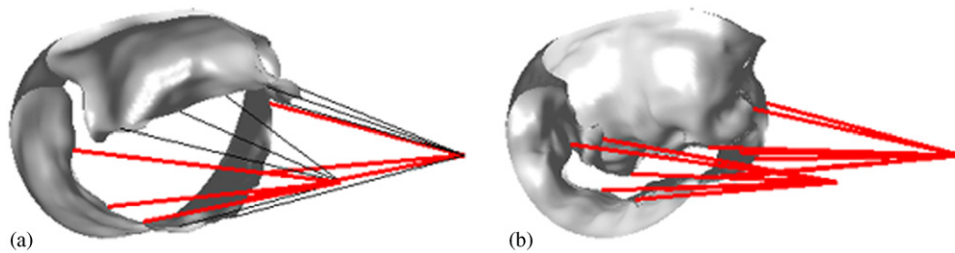


Fig. 14. On closure, a mechanically unrealistic crimping of the valve leaflets occurs (right).
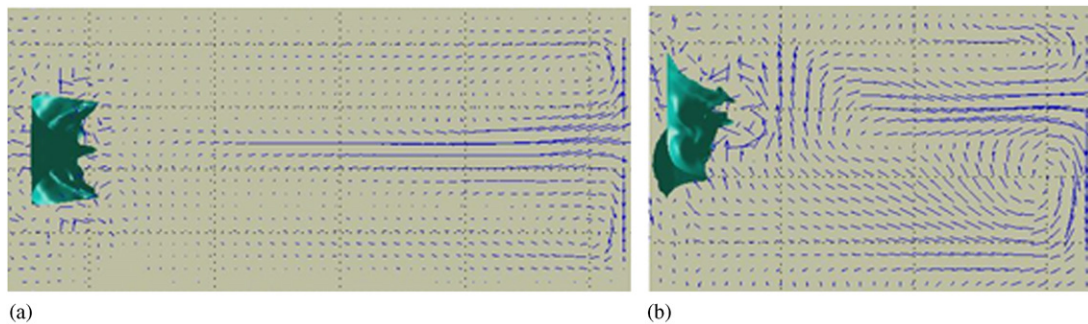


Fig. 15. (a) The aortic prosthesis develops a central jet and symmetric vortices and (b) The mitral prosthesis deflects the flow introducing an asymmetry into vortices.

similarly to the native valve in terms of its flow dynamics and should yield improved haemodynamic performance over existing prostheses.

## 4. Discussion

An effective computational approach using the IB method has been developed to study heart prostheses. A purpose built computational code has been written to efficiently model any multileaflet elastic structure of arbitrary geometry, which can include elastic chorded reinforcements in its surface. In this paper, only artificial valves are considered. However, the method could readily be applied to model native valves. The IB code has also been extended for static analysis. This enables comparative validation of the mechanical properties of an IB 'fibre model' with an FEM shell model. Validations presented here have shown good quantitative agreement with both ANSYS and experimental

data. Indeed, steady analysis may be a useful preliminary tool to highlight regions of the valve prone to critical strains, and to investigate the mechanical effects of different chordal configurations in the bileaflet mitral valve design. Dynamic analysis yields results that are consistent with experiment, and may be used to explore the effects that modifications to the valve design have on the dynamics of the fluid. Importantly, we have seen that our new mitral design has better physiological flow characteristics compared with the aortic valve when used for the mitral position.

The prosthesis designs have relatively thin flexible leaflets. Numerical simulations of the thin structures using shells typically run into the difficulty of "numerical locking" in obtaining converged solutions. IB model shows its advantages in modelling thin leaflets, while in the ANSYS model, increased thickness together with a reduced Young's model needs to be used to help to obtain a converged solution within reasonable time. As a result, the deformation obtained from the ANSYS model is slightly lower than it should be, and it is slightly higher from the IB predictions. However, they both provided good agreement with the experimental measurements for a range of physiological pressures. The biggest advantage of IB model is its readiness and effectiveness in the dynamic simulations compared with any commercially available packages.

The current IB model still represents the solid simply by providing the stretching stiffness in the fibre directions. Surprisingly, this simplified approach has yielded quite good quantitative agreements with experiments both in static and dynamic cases. However, it is clear that in order to improve its predictive power, bending stiffness needs to be incorporated. The current IB models tend to bend excessively or crimp unrealistically in the fluid flow. This mechanical limitation accounts for some of the minor discrepancies between predicted and measured pressure gradients across the valves. Examples are the delayed opening times attributed to leaflets inflating prior to opening, and the slower closing times due to the absence of bending forces. Furthermore, the absence of bending in the IB model implies that the mitral prosthesis will remain in a more opened configuration as the flow rate fluctuates, thus the secondary pressure gradient peak will be lower than that observed experimentally, i.e. computational pressure gradients are less sensitive to variations in the flow rate if the valve geometry itself is less sensitive to variations in the flow rate.

One particular problem, inherent to the current version of IB model is that for effective valve opening to occur, a physical separation between the leaflets must exist at the beginning of the opening phase. If there is no separation, the leaflets will simply not open, i.e. fibre points (in different leaflets) that share identical spatial coordinates, will have equal spatial coordinates at all successive times. If the separation is too small (with respect to the resolution of the fluid mesh), an artificial sticking effect may be introduced between unconnected fibres in closely separated regions, such as between the closed valve leaflets. Consequently, unrealistically high-pressure gradients may be required to open the valve if the fluid mesh is not fine enough with respect to the "artificial" edge separation. The same problem applies for the contact area in the static analysis: no real physical contact can be modelled in the IB model, the gap between the contact is limited by the fluid resolution between the contacts surfaces we can achieve. This is a problem that is difficult to resolve using the current IB methodology. For the initial opening case, the problem can be dealt with in two ways: the IB model can be modified to insert a separation between the leaflets or the resolution of the fluid mesh may be increased. The first approach requires slight modifications to the valve design and it may not then continue to accurately reflect the mechanical and dynamic behaviour of the valve. The second approach greatly increases computational time. Clearly, one way of increasing the mesh resolution in the vicinity of the valve leaflets is to use a non-uniform fluid mesh that has high resolution in the vicinity of the valve leaflet free edges, particularly during the opening and closing phase. However, the drawback of this is that the FFT could not be applied to solve the fluid equations, thus reducing the computational efficiency.

## 5. Conclusions

We have developed an IB code that is suitable for both static and dynamic modelling of heart valves. The IB model has been successfully applied to study the mechanical behaviour of trileaflet and newly designed chorded mitral prostheses, and results are validated with both ANSYS and experimental studies. Dynamic simulations of the valves in the whole opening and closing cycles are carried out for four different flow rates. Consistent results are obtained in terms of pressure gradient across the valves. In addition, the mitral valve is shown to have better haemodynamic behaviour compared with the aortic valve for the mitral position. It demonstrated that IB has advantages for simulating fluid–structure interactions of thin valves with large deformation and complicated geometries. Some limitations of the current IB method are also discussed. Further development of IB model to rectify this will result in a more effective tool for valve design.

## Appendix A

An undeformed *covariant* set of base vectors $(\mathbf{g}_1^E, \mathbf{g}_2^E, \mathbf{g}_3^E)$ is defined, where $\mathbf{g}_1^E$, $\mathbf{g}_2^E$ are parallel to fibres 1 and 2, respectively, i.e.

$$\mathbf{g}_1^E = ((\mathbf{p}_{(E,1)}^2 - \mathbf{p}_{(E,1)}^1)/|(\mathbf{p}_{(E,1)}^2 - \mathbf{p}_{(E,1)}^1)|,$$
$$\mathbf{g}_2^E = ((\mathbf{p}_{(E,2)}^2 - \mathbf{p}_{(E,2)}^1)/|(\mathbf{p}_{(E,2)}^2 - \mathbf{p}_{(E,2)}^1)|, \qquad (9)$$

and $\mathbf{g}_3^E$ is the unit vector perpendicular to $\mathbf{g}_1^E$ and $\mathbf{g}_2^E$, i.e. $\mathbf{g}_3^E = \mathbf{g}_1^E \wedge \mathbf{g}_2^E$. A contravariant set of base vectors, $\mathbf{g}^j$ can be determined such that $\mathbf{g}_i \cdot \mathbf{g}^j = \delta_i^j$. Following the deformation, the deformed basis vectors $(\mathbf{G}_1^E, \mathbf{G}_2^E, \mathbf{G}_3^E)$ may similarly be calculated, i.e.

$$\mathbf{G}_1^E = ((\mathbf{p}_{(E,1)}^2(t) - \mathbf{p}_{(E,1)}^1(t))/|(\mathbf{p}_{(E,1)}^2(t) - \mathbf{p}_{(E,1)}^1(t))|,$$
$$\mathbf{G}_2^E = ((\mathbf{p}_{(E,2)}^2(t) - \mathbf{p}_{(E,2)}^1(t))/|(\mathbf{p}_{(E,2)}^2(t) - \mathbf{p}_{(E,2)}^1(t))|, \qquad (10)$$

and $\mathbf{G}_3^E$ is defined to be the unit vector perpendicular to the fibres. The undeformed (deformed) covariant metric tensor may be calculated $g_{ij} = \mathbf{g}_i \cdot \mathbf{g}_j$ ($G_{ij} = \mathbf{G}_i \cdot \mathbf{G}_j$). The strain tensor may be expressed in terms of the standard Cartesian basis via $\varepsilon_{ij}^E = \tilde{\varepsilon}_{mn}^E (\mathbf{g}^m \cdot \mathbf{e}_i)(\mathbf{g}^n \cdot \mathbf{e}_j)$ where $\tilde{\varepsilon}_{ij}^E = (\mathbf{G}_i^E \cdot \mathbf{G}_j^E - \mathbf{g}_i^E \cdot \mathbf{g}_j^E)/2$ (see Bathe, 1996).

## References

Arthurs, K.M., Moore, L.C., Peskin, C.S., Pitman, E.B., Layton, H.E., 1998. Modeling arteriolar flow and mass transport using the immersed boundary method. Journal of Computer Physics 147, 402.

Bathe, K.J., 1996. Finite Element Procedures. Prentice Hall, Englewood Cliffs, NJ.

Beyer, R.P., 1992. A computational model of the cochlea using the immersed boundary method. Journal of Computer Physics 98, 145.

Bernacca, G.M., Mackay, T.G., Wilkinson, R., Wheatley, D.J., 1995. Calcification and fatigue failure in a polyurethane heart valve. Biomaterials 16, 279–285.

Bernacca, G.M., Mackay, T.G., Wheatley, D.J., 1996. In vitro function and durability of a polyurethane heart valve: material considerations. Journal of Heart Valve Disease 5, 538–542.

Bernacca, G.M., Mackay, T.G., Wilkinson, R., Wheatley, D.J., 1997a. Polyurethane heart valves: fatigue failure, calcification and polyurethane structure. Journal Of Biomedical Materials Research 34, 371–379.

Bernacca, G.M., Mackay, T.G., Gulbransen, M.J., Donn, A.W., Wheatley, D.J., 1997b. Polyurethane heart valve durability: effects of leaflet thickness. International Journal Of Artificial Organs 20, 327–331.

Bernacca, G.M., Raco, L., Mackay, T.G., Wheatley, D.J., 1999. Durability and function of a polyurethane heart valve after six months in vivo. Artificial Organs 23 (7), 665.

Bernacca, G.M., Straub, I., Wheatley, D.J., 2002. Mechanical and morphological study of biostable polyurethane heart valve leaflets explanted from sheep. Journal Of Biomedical Materials Research 61, 138–145.

Bernacca, G.M., McColl, J.H., Wheatley, D.J., 2004. Comparison of prosthetic valve hydrodynamic function: objective testing using statistical multilevel modeling. Journal of Heart Valve Disease 13, 467–477.

Chapelle, D., Bathe, K.J., 2003. The Finite Element Analysis of Shells—Fundamentals. Springer, Berlin.

Chapelle, D., 2005. Fundamental and applicative challenges in the modelling and computations of shells. Proceedings of the Third MIT conference on Computational Mechanics, pp. 5–9.

Daebritz, S.H., Sachweh, J.S., Hermanns, B., et al., 2003. Introduction of a flexible polymeric heart valve prosthesis with special design for mitral position. Circulation 108 (Suppl. II), II-134–II-139.

Fauci, L.J., Peskin, C.S., 1988. A computational model of aquatic animal locomotion. Journal of Computational Physics 77, 85.

Fisher, J., Jack, G.R., Wheatley, D.J., 1986. Design of a function test apparatus for prosthetic heart valves. Initial results in the mitral position. Clinical Physics And Physiological Measurement 7, 63–73.

Fogelson, A.L., 1984. A mathematical model and numerical method for studying platelet adhesion and aggregation during blood clotting. Journal of Computational Physics 56, 111.

King, M.J., Corden, J., Dadiv, T., Fisher, J., 1996. A three-dimensional, time dependent analysis of flow through a bileaflet mechanical heart valve: comparison of experimental and numerical results. Journal of Biomechanics 29 (5), 609–618.

Kunzelman, K.S., Cocharan, M.D., 1993. Finite element analysis of the mitral valve. Journal of Heart Valve Disease 2, 326–340.

Kunzelman, K.S., Reimink, B.S., Verrier, E.D., Cochran, R.P., 1996. Replacement of mitral valve posterior chordae tendineae with expanded polytetraflouroethylene suture. Journal Of Cardiac Surgery 11, 136–145.

Mackay, T.G., Wheatley, D.J., Bernacca, G.M., Hindle, C.S., Fisher, A.C., 1996a. New polyurethane heart valve prosthesis: design, manufacture and evaluation. Biomaterials 17, 1857–1863.

Mackay, T.G., Bernacca, G.M., Wheatley, D.J., Fisher, A.C., Hindle, C.S., 1996b. In vitro function and durability assessment of a polyurethane heart valve prosthesis. Artificial Organs 20, 1017–1025.

McQueen, D.M., Peskin, C.S., 1983. Computer-assisted design of pivoting-disc prosthetic mitral valves. Journal Of Thoracic And Cardiovascular Surgery 86, 126–135.

McQueen, D.M., Peskin, C.S., 1997. Shared-memory parallel vector implementation of the immersed boundary method for the computation of blood flow in the beating mammalian heart. Journal Of Supercomputing 11, 213.

McQueen, D.M., Peskin, C.S., 1985. Computer-assisted design of butterfly bileaflet valves for the mitral position. Scandinavian Journal Of Thoracic And Cardiovascular Surgery 19, 139–148.

Peskin, C.S., 1972. Flow patterns around heart valves: a numerical method. Journal of Computational Physics 10, 252.

Peskin, C.S., 1977. Numerical analysis of blood flow in the heart. Journal of Computational Physics 25, 220.

Peskin, C.S., 2002. The Immersed boundary method. Acta Numerica 11, 479–517.

Peskin, C.S., McQueen, D.M., 1989. A three dimensional computational method for blood flow in the heart 1. Immersed elastic fibres in a viscous incompressible fluid. Journal of Computational Physics 81, 372–405.

Peskin, C.S., McQueen, D.M., 1995. A general method for the computer simulation of biological systems interacting with fluids. Symposia Of The Society For Experimental Biology 49, 265.

Peskin, C.S., McQueen, D.M., 1996. Fluid dynamics of the heart and its valves. In: Othmer, H.G., Adler, F.R., Lewis, M.A., Dallon, J.C. (Eds.), Case Studies in Mathematical Modeling: Ecology, Physiology, and Cell Biology. Prentice-Hall, Englewood Cliffs, NJ, p. 309.

Stockie, J.M., Green, S.I., 1998. Simulating the motion of flexible pulp fibres using the immersed boundary method. Journal of Computational Physics 147, 147–165.

Watton, P.N., Luo, X.Y., Wang, X., Bernacca, G.M., Molloy, P., Wheatley, D.J., 2004a. Static and dynamic modelling of heart valves using the immersed boundary method. Presented at the 14th European Congress of Biomechanics, 's-Hertogenbosch, July 2004a.

Watton, P.N., Luo, X.Y., Singleton, R., Wang, X., Bernacca, G.M., Molloy, P., Wheatley, D.J., 2004b. Modelling chorded prosthetic mitral valves using the immersed boundary method. Proceedings of the 26th Annual International Conference of the IEEE Engineering in Medicine and Biology Society. San Francisco, California, pp. 3745–3748.

Wheatley, D.J., 2002. Mitral valve prosthesis, Patent number WO03037227.

Wheatley, D.J., Raco, L., Bernacca, G.M., Sim, I., Belcher, P.R., Boyd, J.S., 2000. Polyurethane: material for the next generation of heart valve prostheses? European Journal Of Cardio-Thoracic Surgery 17, 440–447.